ACS Catalysis

Research Article

pubs.acs.org/acscatalysis

Partial Oxidation of Methane to Syngas Over γ-Al_2O_3-Supported Rh Nanoparticles: Kinetic and Mechanistic Origins of Size Effect on Selectivity and Activity

Vita A. Kondratenko, Claudia Berger-Karin, and Evgenii V. Kondratenko*

Leibniz-Institut für Katalyse e.V. an der Universität Rostock Albert-Einstein-Strasse 29 a, D-18059 Rostock, Germany

Supporting Information

ABSTRACT: A series of supported Rh/γ-Al_2O_3 catalysts with an overall metal loading of 0.005 wt % was synthesized by impregnation of γ-Al_2O_3 with a toluene solution containing colloidally prepared well-defined (1.1, 2.5, 2.9, 3.7, and 5.5 nm) Rh nanoparticles (NP). The size of NP was not found to change after their deposition on γ-Al_2O_3 and even after performing partial oxidation of methane (POM) to synthesis gas at 1073 K for 160 h on stream. Apparent CO formation turnover rates and CO selectivity strongly decrease with an increase in this size. Contrarily, the overall scheme of POM is size-independent, i.e. CO and H_2 are mainly formed through reforming reactions of CH_4 with CO_2 and H_2O at least under conditions of complete oxygen conversion. The size effect on the activity and selectivity was related to the kinetics of interaction of CH_4, O_2, and CO_2 with Rh/γ-Al_2O_3 as concluded from our microkinetic analysis of corresponding transient experiments in the temporal analysis of products reactor. The rate constants of CH_4, O_2, and CO_2 activation decrease with an increase in the size of supported Rh NP thus influencing both primary (methane combustion) and secondary (reforming of methane) pathways within the course of POM.

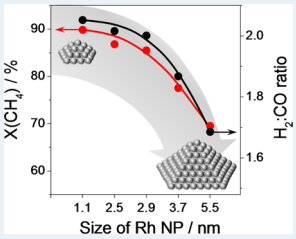

KEYWORDS: *nanoparticles, Rh, partial methane oxidation, syngas, mechanism, kinetics, TAP reactor*

INTRODUCTION

Catalytic partial oxidation of methane (POM) to CO and H_2 is an attractive alternative to the industrially applied steam reforming of methane (SRM) owing to exothermicity and the ratio of H_2/CO of 2, which is desired for large-scale methanol and Fischer−Tropsch (FT) syntheses. Consequently, POM has been extensively studied.[1−3] Alike to SRM, POM is catalyzed by the metals of group VIII. Their activity order is quite similar for these both reactions: Rh ≈ Ru > Ni ≥ Ir ≥ Pt, Pd.[2,4] Irrespective of the active metal, the turnover frequency of methane conversion in the SRM reaction was reported to decline with a decrease in metal dispersion.[4−7] This was explained by the structural sensitivity of methane activation being the rate-limiting step.[4,5,8] The cleavage of the C−H bond in the CH_4 molecule occurs predominantly on the edge and corner metal atoms, the fractional density of which increases with rising metal dispersion.[5,9−11]

Recently, Chin et al.[10] carried out a thorough experimental and theoretical analysis of relevant kinetic pathways in the course of POM over supported Pt-containing catalysts with different metal dispersion. Depending on the O_2/CH_4 ratio, various kinetically relevant elementary reaction steps were identified. For the ratios between 0.17 and 2, i.e. in the front of the catalyst bed, these steps were activation of CH_4 and O_2. With a further decrease in this ratio, CH_4 activation became kinetically irrelevant but started to dominate after gas-phase O_2 was completely consumed. In this regime, methane reforming with CO_2 and H_2O results in the formation of syngas. However, the effect of Pt dispersion on product selectivity was not analyzed. Moreover, that study was performed at temperatures up to 900 K, which are below typical POM temperature. Besides, the catalysts tested were prepared according to classical impregnation methods resulting in a broad distribution of metal particle size. Recently, Berger-Karin et al.[12] demonstrated that supporting well-defined (∼1.3 nm) colloidally prepared Rh nanoparticles (NP) on γ-Al_2O_3 with a metal loading as low as only 0.005 wt % resulted in an active and stable POM catalyst. No catalyst deactivation was observed over 160 h on-stream even at 1073 K because NP did not change their size owing to their very low apparent surface density. Thus, such catalysts appear to be very suitable for studying the effect of the size of supported Rh NP on their POM performance.

On the basis of the above background, we prepared well-defined (1.1, 2.5, 2.9, 3.7, and 5.5 nm) Rh NP and deposited them on γ-Al_2O_3. Their POM activity and selectivity at different degrees of methane conversion were tested at 1073 K under ambient-pressure continuous-flow conditions. To derive fundamental insights into the effect of Rh NP size on their POM performance, we additionally investigated mechanistic and kinetic aspects of CH_4−O_2, CH_4−CO_2, CH_4, CO_2, and O_2 interactions with Rh/γ-Al_2O_3 by means of transient analysis of products with microsecond time resolution under vacuum conditions. These experiments were rigorously evaluated for

Received: February 25, 2014
Revised: August 1, 2014
Published: August 5, 2014

   dx.doi.org/10.1021/cs5002465 | ACS Catal. 2014, 4, 3136−3144

determining rate constants of individual reaction steps of CH_4, O_2, and CO_2 activation.

2. EXPERIMENTAL SECTION

2.1. Preparation, Characterization, and Deposition of Rh Nanoparticles. Rhodium^{III} chloride hydrate ($RhCl_3{\cdot}nH_2O$, 38−40% Rh, Aldrich) and ethylene glycol (EG, 99.8%, Aldrich, anhydrous) were employed without further purification. γ-Al_2O_3 (SASOL, Puralox NWa 155, 151 m^2/g) was used as support. The Rh content of the colloidal solution was fixed on the basis of the $RhCl_3{\cdot}nH_2O$ precursor concentration of 37.4 wt % Rh determined by inductively coupled plasma optical emission spectrometry.

The method of Rh NP synthesis was adopted from ref 13. Briefly, a solution of 10 mL EG and 50 μL of aqueous 1 M NaOH was heated to 388 K. Under continuous stirring, a solution of 5 mM $RhCl_3{\cdot}nH_2O$ and 90 mM (related to monomer, M_W = 111.14 $g{\cdot}mol^{-1}$) polyvinylpyrrolidon (PVP) in EG/water (9:1) was added at 2.43 $mL{\cdot}h^{-1}$. To obtain NP sizes of 2.5, 2.9, 3.7, or 5.5 nm, 4.86, 9.72, 14.58, or 43.74 mL of Rh-PVP solution were used, respectively. To synthesize 1.1 mm Rh NP, 4.86 mL of the Rh-PVP solution were added immediately to 10 mL EG and 250 μL of aqueous 1 M NaOH and stirred at 388 K for 2 h.

To minimize coverage of metal with stabilizer residues, a phase transfer of Rh NP in EG solution was carried out; PVP was replaced by short-chained dodecylamine (DDA) in toluene. For preparation of supported catalysts, 3.0 g of γ-Al_2O_3 was suspended in 10 mL toluene at room temperature. Hereafter, the DDA-toluene solution of Rh NP was added dropwise to the suspension of γ-Al_2O_3. The obtained mixture was stirred for 3 h until the organic phase became colorless. The solid was separated by centrifugation and then dried at 323 K for 72 h.

The size and distribution of Rh NP in solution was determined by small-angle X-ray scattering (SAXS). The measurements were carried out on a Kratky-type instrument (SAXSess, Anton Paar, Austria) operated at 40 kV and 50 mA in slit collimation using a two-dimensional CCD detector. Further details can be found in ref 12.

An overall number of surface Rh atoms in supported catalysts was determined from N_2O pulse experiments performed at 573 K under transient vacuum conditions (section 2.3). The catalysts (40 mg; sieve fraction of 250−355 μm) were initially treated in a flow of H_2 at 1073 K for 1 h. In these pulse experiments, N_2O decomposed to N_2 and an irreversibly adsorbed oxygen atom. Gas-phase O_2 was not observed. For each catalyst, the experiments were repeated five times using a fresh sample. The following atomic mass units (AMUs) were monitored for identification of feed components and reaction products by means of an online mass spectrometer: 44.0 (N_2O), 30.0 (N_2O), 28.0 (N_2 and N_2O), 32.0 (O_2), 40.0 (Ar), and 4.0 (He). N_2O (medical, Air Liquide, purity ≥98%) and Ar (5.0) were used without further purification.

2.2. Steady-State Catalytic Experiments. Catalytic tests were carried out in plug flow fixed-bed quartz reactors (i.d. 4 mm) at atmospheric pressure using a feed mixture containing 29 vol % methane in air (CH_4/O_2 = 2). For determining on-stream stability of catalysts, the experiments were performed at 1073 K for 160 h with a gas hourly space velocity (GHSV) of 24,640 h^{-1} using 30 mg (sieve fraction of 250−450 μm) of each catalyst. To derive insights into the effect of CH_4 conversion on product selectivity, GHSV was varied. For all tests, the catalysts were initially heated up to 873 K in an Ar flow with 5 K min^{-1}. Hereafter, the methane−air mixture was fed to the reactor, and temperature was increased to 1073 K with 5 K min^{-1}. This temperature was held constant for 160 h. The feed components and the reaction products were analyzed by an online gas chromatograph (Agilent 7890) equipped with PLOT/Q (for CO_2), AL/S (for hydrocarbons), and Molsieve 5 (for H_2, O_2, N_2, and CO) columns as well as flame ionization and thermal conductivity detectors. The conversion of CH_4 and O_2 was calculated from the inlet and outlet concentrations of CH_4 and O_2. The selectivity to H_2O, H_2, CO, and CO_2 was calculated from their outlet concentrations.

2.3. Transient Experiments. Transient studies were performed in the temporal analysis of products (TAP) reactor, a time-resolved technique with a resolution of approximately 100 μs. The TAP reactor system has been described in detail elsewhere.[14,15] The catalyst (20 mg; sieve fraction of 250−355 μm) was packed between two layers of quartz of the same particle size within the isothermal zone of a quartz-tube microreactor. Before transient experiments were started, the reactor was evacuated at room temperature and then heated in vacuum to 1073 K with a rate of 10 $K{\cdot}min^{-1}$. Hereafter, the catalyst was treated by O_2 pulses until CO and CO_2 formed via oxidation of organic compounds remaining from catalyst preparation were not observed.

For analyzing O_2, CO_2, and CH_4 interactions with Rh/γ-Al_2O_3, various pulse experiments were performed at 1073 K using O_2/Ar = 1:1, CH_4/Ar = 1:1, CH_4/O_2/Ar = 2:1:2, CH_4/CO_2/Ar = 1:1:1, and CO_2/Ar = 1:1 mixtures. An overall pulse size was around 10^{15} molecules. Under such conditions (Knudsen diffusion regime), any collisions between gas-phase species are minimized, and therefore, pure heterogeneous reaction steps were analyzed.

The reaction mixtures were prepared using Ar (5.0), O_2 (4.5), CO_2 (4.5), and CH_4 (3.5) without additional purification. A quadrupole mass spectrometer (HAL RC 301 Hiden Analytical) was applied for quantitative analysis of feed components and reaction products. The following AMUs were used for mass-spectrometric identification of different compounds: 44 (CO_2), 32 (O_2), 28 (CO, CO_2,), 18 (H_2O), 15 (CH_4), 2 (H_2, CH_4), and 40 (Ar). Pulses were repeated 10 times for each AMU and averaged to improve the signal-to-noise ratio. The concentrations of feed components and reaction products were determined from the respective AMUs using standard fragmentation patterns and sensitivity factors. On the basis of these calibration data, the signals of CO and H_2 were corrected in order to subtract the contributions from CO_2 and CH_4, respectively.

2.4. Kinetic Evaluation of Transient Experiments. Kinetic evaluation of transient experiments, i.e. fitting experimental data to various kinetic models, was performed according to ref 16. The TAP microreactor is described as a one-dimensional pseudohomogeneous system divided into three different zones, which are represented by the catalyst layer sandwiched between two layers of inert material.

Outside the catalyst layer, the mass balances for each species "i" can be written as follows:

$$\frac{\partial C_i}{\partial t} = D^{\mathrm{eff}}_{\mathrm{Knudsen}} \cdot \frac{\partial^2 C_i}{\partial x^2} \text{ for gas-phase species} \quad (1)$$

$$\Theta_i = 0 \text{ for surface species} \quad (2)$$

In the catalyst zone, the reaction term is included in the mass balance:

$$\frac{\partial C_i}{\partial t} = D^{\mathrm{eff}}_{\mathrm{Knudsen}} \cdot \frac{\partial^2 C_i}{\partial x^2} + \sum_j \rho_{\mathrm{cat}} \nu_{ij} r_j \text{ for gas-phase species} \quad (3)$$

$$\frac{\partial \Theta_i}{\partial t} = \sum_j \frac{\nu_{ij} r_j}{C_{\mathrm{total}}} \text{ for surface species} \quad (4)$$

with

$$r_j = k_j \prod_l C_l^{n_l} \prod_m \theta_m^{n_m} \quad (5)$$

where

$$0 \le n_l \le 1,\ 0 \le n_m \le 2$$

where $\Theta_i = C_i/C_{\mathrm{total}}$, C_{total} is total concentration of surface species and $D^{\mathrm{eff}}_{\mathrm{Knudsen}}$ is the effective Knudsen diffusion coefficient of gas-phase species.

The resulting partial differential equations are transformed into coupled ordinary differential equations by a spatial approximation and then integrated by numerical routine PDEONE.[17] The search for kinetic parameters (reaction constants) was performed in a wide range of possible values (10^{-4}−10^6) using first a Genetic[18] and then the Nelder−Mead Simplex algorithms.[19] The former algorithm was used

dx.doi.org/10.1021/cs5002465 | ACS Catal. 2014, 4, 3136−3144

to find the best starting parameters for the Simplex algorithm, by which the final parameters were estimated.

For the best kinetic model, the estimated parameters were validated by applying correlation and sensitivity analyses. In case of correlating parameters, they cannot be determined individually, i.e. either product or ratio of two such parameters is definitively obtained. The sensitivity analysis provides information on the significance of the parameter for the objective function. This is helpful for avoiding model over-parameterization.

3. RESULTS AND DISCUSSION

3.1. Characterization of Rh nanoparticles. Size and distribution of Rh NP in solution were analyzed by SAXS. The scattering profiles obtained are shown in Figure S1 (a) in the Supporting Information (SI). In order to determine the volume-weighted distribution function $D_v(R)$, the SAXS profiles were fitted (solid lines in Figure S1 (a) in the SI) according to ref.[20,21] using the program GIFT.[22] The resulting $D_v(R)$ profiles are presented in Figure S1 (b) in the SI. The estimated mean diameters of Rh NP amount to 1.1, 2.5, 2.9, 3.7, and 5.5 nm. As shown in our previous study,[12] the volume-weighted particle size distribution obtained by SAXS does not significantly differ from the number-weighted distribution gained from TEM. However, due to very low metal loading (0.005 wt %) in Rh/γ-Al_2O_3 catalysts, it is difficult to ascertain accurately the size distribution of supported Rh NP from microscopic images. Therefore, we performed titration experiments with N_2O to determine an overall number of available surface Rh atoms (for experimental details see section 2.1). In these experiments, N_2O decomposed to N_2 and adsorbed oxygen atoms, while gas-phase O_2 was not observed. N_2O conversion and the corresponding amount of formed N_2 decreased with increasing number of N_2O pulses (Figure S2 in the SI) and reached zero when all active sites for N_2O decomposition were blocked by adsorbed oxygen species formed from N_2O. It is worth mentioning that formation of subsurface oxygen can be neglected in our experiments owing to very low exposure of catalysts to N_2O. As determined in an earlier study,[23] only 5% monolayer of surface oxygen atoms can occupy subsurface sites at the exposure to O_2 of 10^5 Langmuir, i.e. 13.3 Pa·s. The maximal exposure value to N_2O in the present study was only 0.16 Pa·s during each N_2O pulse.

According to the stoichiometry of N_2O decomposition, the amount of converted N_2O or formed N_2 is equal to the amount of oxygen species on the surface of Rh NP. Previous studies on O_2, NO, and NO_2 adsorption on Rh(111) between 273 and 525 K[24] established that one O atom adsorbs on two Rh atoms. Considering this information, we estimated an averaged number of surface Rh atoms (Figure 1). Additionally, we calculated such a number based on the size of Rh NP determined by SAXS and their geometry as suggested in refs 11,25. The respective values are also presented in Figure 1. A quite good match between two different approaches is obvious. This result together with previous studies[26−28] demonstrates that the size of noble metal NP prepared by the colloidal approach did not significantly change after their deposition from the solution onto γ-Al_2O_3.

3.2. POM Performance of Supported Differently Sized Rh Nanoparticles. The effect of Rh NP size (1.1, 2.5, 2.9, 3.7, and 5.5 nm) on their activity and selectivity in POM was studied under steady-state conditions. The catalysts were applied without any reductive treatment and tested at 1073 K using a feed of 29 vol % methane in air (CH_4/O_2 = 2:1) with GHSV of 24,640 h^{-1}. After initial activation they revealed stable

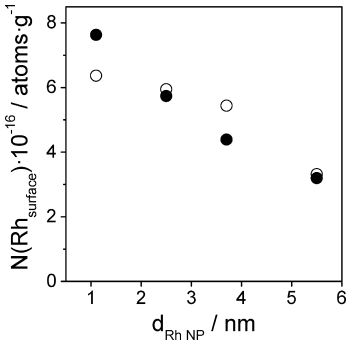

Figure 1. Comparison between number of surface Rh atoms determined from N_2O decomposition tests (○) and theoretically estimated according to ref 25 (●).

CO yield during at least 160 h on stream Figure 2a. The highest CO yield of 86% and the highest CH_4 conversion of 90% were

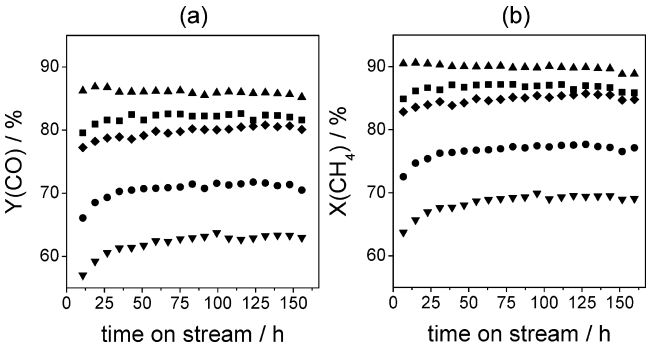

Figure 2. Time on stream (a) CO yield and (b) CH_4 conversion over Rh(0.005 wt %)/γ-Al_2O_3 with Rh NP of (▲) 1.1, (■) 2.5, (♦) 2.9, (●) 3.7, and (▼) 5.5 nm. Reaction conditions: 1073 K, 29% CH_4 in air, GHSV of 24,640 h^{-1}.

observed over the catalyst with the smallest NP (Figure 2). Both the yield and the conversion decreased with an increase in NP size; the catalyst with Rh NP of 5.5 nm showed the worst catalytic characteristics of 63 and 70%, respectively. Importantly, the decrease in the yield is not simply due to lower conversion but due as well to lower selectivity to CO (Figure S3 in the SI). The selectivity to hydrogen is also influenced by NP size as evidenced by a decrease in the ratio of H_2/CO from 2 to 1.7 with rising size from 1.1 to 5.5 nm (Figure S3 in the SI). Since this ratio depends on methane conversion, it can be suggested that the formation of CO and H_2 proceeds through different reaction pathways. This statement is supported by the below results of steady-state tests in the range of methane conversion from 30 to 80% and mechanistic analysis described in section 3.3.

Appraising the results from Figure 2, two important conclusions should be highlighted: (i) irrespective of NP size, no catalyst deactivation is observed, and (ii) CH_4 conversion and CO selectivity decrease with the size of Rh NP. On the basis of these two experimental facts, we can safely conclude that NP did not change their original size over 160 h on POM stream at 1073 K. Otherwise, CH_4 conversion would decrease with time on stream. Therefore, the dissimilar POM performance of differently sized supported Rh NP should be governed by mechanistic and/or kinetic factors.

To check if the reaction mechanism of POM depends on NP size, we performed steady-state tests at different degrees of

dx.doi.org/10.1021/cs5002465 | ACS Catal. 2014, 4, 3136−3144

methane conversion. In these experiments, oxygen was completely consumed even at 30% methane conversion. This is in agreement with previous studies of Schmidt et al.,[29,30] who performed spatially resolved measurements of POM over Rh(6 wt %)/α-Al_2O_3 and Pt or Rh foam catalysts. Taking into account the feed ratio of CH_4/O_2 of 2, such misbalance in the consumption of these feed components can only be explained by the fact that CH_4 was oxidized by gas-phase O_2 to CO_2 and H_2O but not to CO and H_2. The effect of CH_4 conversion on the selectivity to H_2, H_2O, CO, and CO_2 is shown in Figure 3.

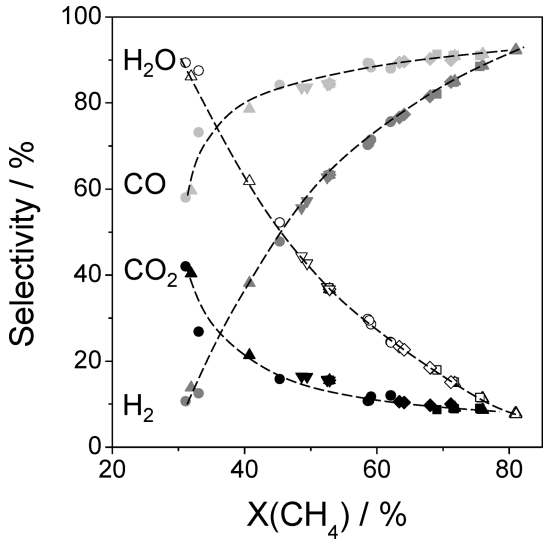

Figure 3. H_2, H_2O, CO, and CO_2 selectivity at 1073 K versus CH_4 conversion over Rh(0.005 wt %)/γ-Al_2O_3 with Rh NP of (▲) 1.1, (■) 2.5, (♦) 2.9, (●) 3.7, and (▼) 5.5 nm.

Irrespective of NP size, CO_2 selectivity decreases with an increase in the conversion, while CO selectivity rises. A corresponding dependence is also valid for the selectivity to H_2O and H_2. It is worth mentioning that the selectivity profiles of H_2 and CO strongly differ from each other and their ratio increases with methane conversion. Schmidt et al.[29,30] have also observed that H_2 formation is stronger influenced by the conversion than CO. If the direct oxidation of methane to CO and H_2 were the main route,[31−33] these products would be formed simultaneously, and the difference between their selectivity profiles would be not so obvious. Thus, we can conclude that CO and H_2 are mainly formed through reforming reactions of CH_4 with primarily generated CO_2 and H_2O. CO can also be partly formed directly from CH_4. However, compared to POM over Rh(6 wt %)/α-Al_2O_3 and Pt or Rh foam catalysts, which yielded around 50% CO directly from methane, the reforming route is responsible for at least 85% of CO production over our supported well-defined Rh NP under conditions of complete oxygen conversion. As seen from Figure 3, the yield of CO increases from 18 to 72% with an increase in methane conversion from 30 to 82%. The syngas formation through indirect route was previously observed over Rh powder[18] and different supported Rh catalysts.[34,35]

Since the mechanism of POM is valid for all catalysts irrespective of Rh NP size, we put forward that their distinct POM performance (Figure 2) is due to their different intrinsic activity. This conclusion is supported by the fact that an apparent turnover rate of CO formation strongly decreases with an increase in the size of NP as shown in Figure 4. These values

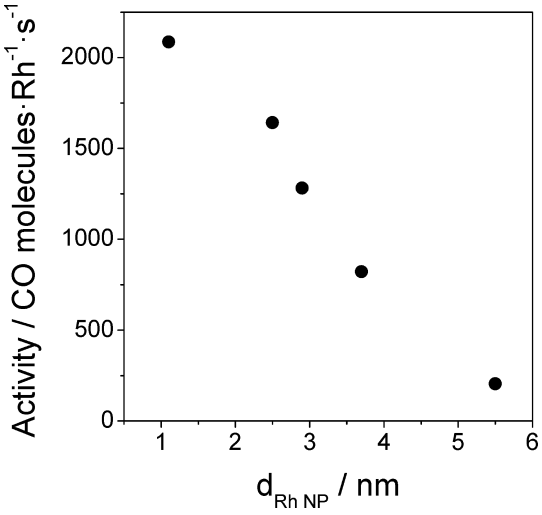

Figure 4. Rh-normalized rate of CO formation at 70% CO yield.

were calculated at 70% CO yield and under consideration of surface concentration of Rh atoms from Figure 1. Owing to the size-independence of the reaction mechanism, such comparison of the catalysts is conceivable despite methane conversion being too high for differential operation.

3.3. Methane Activation over Rh NP in the Absence and the Presence of O_2 or CO_2. CO and H_2 but no CO_2 were observed upon interaction of CH_4 in absence of O_2 or CO_2 with all catalysts. The formation of H_2 is related to decomposition of CH_4 on the surface of metallic Rh NP. However, the presence of CO is surprising because the surface of Rh NP was cleaned from possible adsorbed oxygen species by large H_2 pulses at 1073 K (pulsing was stopped when H_2 was not consumed anymore). In addition, we have used high-purity CH_4 (>99.95%). Therefore, lattice oxygen of Al_2O_3 should be the only source of oxygen. However, only around 0.01% of such species can be removed as estimated from the amount of CO formed. There are two possibilities for CO formation. The first one includes dissociation of gas-phase CH_4 on metallic Rh sites to CH_x and H species. The latter can be oxidized to H_2O by lattice oxygen of Al_2O_3 at the interface of Rh NP and the support. We have previously demonstrated that trace amounts of Rh promote removal of lattice oxygen from Al_2O_3[36] in the course of temperature-programmed catalyst reduction by H_2. So-formed water oxidizes remaining surface CH_x fragments to CO. Alternatively, surface CH_x species can be directly oxidized by lattice oxygen of Al_2O_3. Such a pathway of CO formation was earlier reported for methane oxidation over Rh(1 wt %)/$(Ce_{0.56}Zr_{0.44})O_{2-x}$[37] and Rh/$\gamma$-$A1_20_3$.[34]

When CH_4 and O_2 were simultaneously pulsed, CO_2, CO, and H_2 were observed as reaction products. Figure 5 exemplifies their height-normalized transient responses together with those of Ar and CH_4. In addition, the time scale in this figure was transformed into a dimensionless form as suggested by Gleaves et al.[14] The dimensionless time is defined as $t{\cdot}D_i/L^2$, where t is the measured time, D_i is the effective diffusion coefficient of each component, and L is the reactor length. This transformation is required for proper comparing of the order of appearance of gas-phase components differing in their diffusion velocity due to diverse molecular weights, e.g. H_2, CO, and CO_2. The diffusion coefficients of CH_4, CO_2, CO, and H_2 were calculated from that of Ar according to ref [16]. The diffusion of reaction products was considered from the beginning of the

dx.doi.org/10.1021/cs5002465 | ACS Catal. 2014, 4, 3136−3144

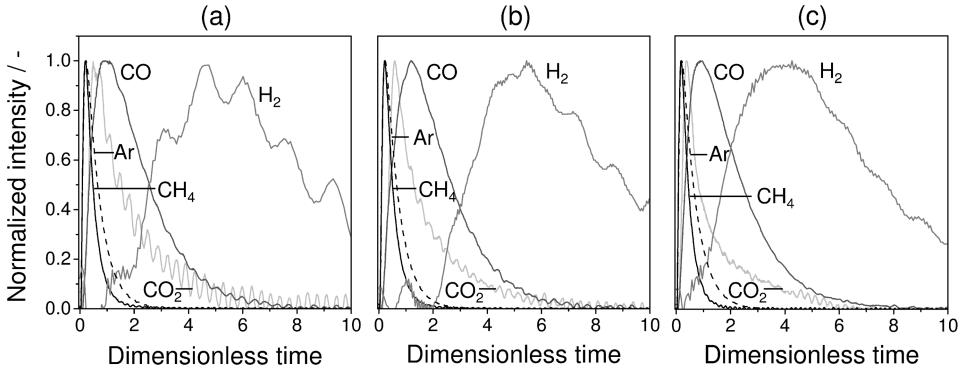

Figure 5. Normalized transient responses of Ar, CH_4, CO_2, CO, and H_2 after pulsing of a $CH_4/O_2/Ar$ = 2:1:2 mixture over Rh(0.005 wt %)/γ-Al_2O_3 with Rh NP of (a) 1.1, (b) 2.9, and (c) 5.5 nm at 1073 K with a total pulse size of ~10^{15} molecules.

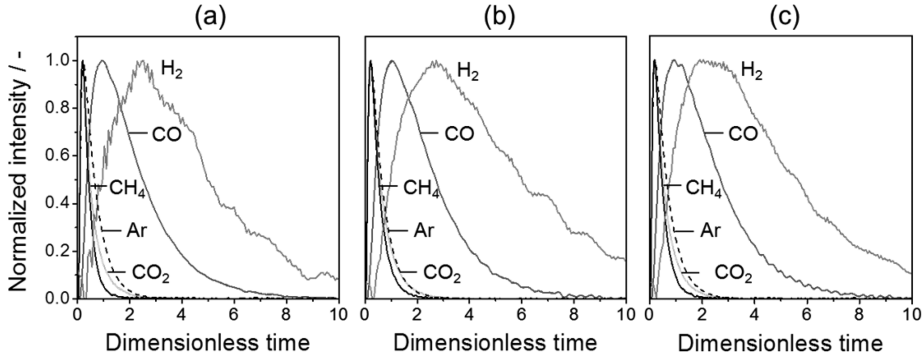

Figure 6. Normalized transient responses of Ar, CH_4, CO_2, CO, and H_2 after pulsing of a $CH_4/CO_2/Ar$ = 1:1:1 mixture over Rh(0.005 wt %)/γ-Al_2O_3 with Rh NP of (a) 1.1, (b) 2.9, and (c) 5.5 nm at 1073 K with a total pulse size of ~10^{15} molecules.

catalyst layer, while the whole reactor length was taken into consideration for the pulsed feed components.

The results shown in Figure 5 clearly demonstrate that the responses of H_2, CO_2, and CO appear after the CH_4 response. The CO response is significantly broader and shifted to longer times compared to the CO_2 response. According to ref 38, desorption of CO and CO_2 from Rh (111) takes place in a similar temperature range and is completed at ~550 K. Since our tests were performed at 1073 K, we can safely reason that the order of appearance of CO and CO_2 responses is not determined by different adsorption/desorption properties of these gas-phase products. Together with the results in Figure 3, it can be concluded that CO_2 is initially formed from CH_4 followed by their reforming reaction to CO. It is noteworthy that CO was not observed when CO_2 was pulsed in the absence of CH_4. Therefore, CO is formed via a reaction of CO_2 with adsorbed H and/or CH_x species. This mechanistic conclusion was also supported by CH_4-CO_2 pulse experiments. The height-normalized responses of Ar, CH_4, CO, and H_2 recorded in these tests are exemplified in Figure 6. As in case of the CH_4-O_2 pulse experiments, the responses of CH_4 and CO_2 are significantly sharper and appear at shorter times than that of CO, i.e. CO_2 is converted to CO as also demonstrated by our steady-state experiments presented in Figure 3. However, transient CH_4-O_2 and CH_4-CO_2 experiments provide some additional kinetic insights. Figures 5 and 6 show that the position and the shape of CO response are very similar in case of CH_4 conversion with O_2 and CO_2. This suggests that the rate of CO formation does not significantly depend on the kind of oxidizing agent. Taking into account this information and the mechanism of POM, i.e. complete oxidation of CH_4 to CO_2 and H_2O followed by reforming reactions of CH_4, we put forward that total combustion of methane should be faster than the reactions leading to syngas.

Another important conclusion from transient CH_4-O_2 and CH_4-CO_2 experiments is related to the formation of H_2. As show in Figures 5 and 6, the maximal H_2 formation is achieved when CO_x formation already declined. This indicates that H_2 is formed not only more slowly but also independently of CO and CO_2. This is in agreement with the steady-state results shown in Figure 3 and with previous studies of POM in the TAP reactor over a commercial Ni-based steam reforming catalyst,[39] differently prepared Rh/Al_2O_3 catalysts,[35] and Pt/$Pr_{0.3}CeZrO_x$.[40]

Taking into account the results presented in Figure 3 and previous literature data for Rh- and Pt-based catalysts,[29,30] H_2 formation should take place in the catalyst zone, where O_2 is completely consumed. In this zone, CO_2, H_2O, and nonreacted CH_4 are the main gas-phase components. CO is formed through steam and dry reforming of CH_4, while H_2 could originate through recombination of surface H species formed on metallic Rh sites from H_2O and CH_4. Owing to weak adsorption of CO on Rh,[38] we can assume that this product desorbs faster than H_2. Thus, the responses of H_2 in Figures 5 and 6 appear after the responses of CO. It should also be noted that H_2 in CH_4-O_2 tests appears after a longer time compared to CH_4-CO_2 tests, while the position of CO responses is very close. This is a strong indication for different reaction pathways leading to H_2 upon CH_4 conversion with O_2 and CO_2. Together with the results shown in Figure 3, a delayed appearance of H_2 response after pulsing of CH_4-O_2 strongly suggests that H_2O formed in the presence of O_2 participates in

dx.doi.org/10.1021/cs5002465 | ACS Catal. 2014, 4, 3136−3144

H_2 formation when O_2 is completely consumed. This process is slower than upon CH_4 conversion with CO_2.

In summary, the above discussion evidences that the sequence of CO and CO_2 formation in the course of POM over Rh/γ-Al_2O_3 does not depend on the size of supported Rh NP. Therefore, the effect of NP size on the activity and selectivity in Figure 2 should be governed by kinetic origins as concluded from the results in Figure 4. To clarify them, we investigated individual reaction pathways of O_2, CO_2, and CH_4 interaction with Rh NP.

3.4. "Fingerprints" of O_2, CH_4, and CO_2 Interaction with Differently Sized Rh NP. The type of CH_4, O_2, and CO_2 interactions with supported Rh NP was elucidated as suggested by Gleaves et al.[14] To this end, the experimental responses of CH_4, O_2, CO_2, and Ar were transformed into a dimensionless form. The modified response of Ar characterizes the solely diffusion process and is called the standard diffusion curve. Such transformation of experimental data helps to discriminate between reversible and irreversible adsorption of reactive gases pulsed together with Ar. Figures S4−S6 (in the SI) compare the dimensionless responses of CH_4, O_2, and CO_2 with the standard diffusion curve. Independent of the presence and the absence of oxidant (O_2 or CO_2), the CH_4 response is situated below the standard diffusion curve and does not cross it (Figure S4 in the SI). This is a "fingerprint" for irreversible interaction of CH_4 with the catalysts.

In contrast to CH_4, O_2 interacts reversibly with Rh NP as concluded from the fact that the dimensionless O_2 response exhibits a broad tailing and crosses the Ar response (Figure S5 in the SI). This tailing indicates that O_2 interaction includes various reversible surface steps. According to theoretical and experimental studies performed on different Rh[41−43] and Pt[44−46] crystal surfaces, O_2 adsorbs reversibly and dissociatively via a molecularly adsorbed oxygen species.

CO_2 also interacts reversibly with Rh NP; the CO_2 response crosses the Ar response as exemplified in Figure S6 in the SI for the catalysts with Rh NP of 1.1 and 5.5 nm. According to previous studies,[47−51] CO_2 adsorbs reversibly and dissociatively below 300 K over different Rh crystal planes. The reaction is structure sensitive, with stepped Rh surfaces showing higher activity toward CO_2 dissociation to adsorbed CO and O species than the smooth (100), (111), and (110) crystal planes.[50] The recombination of adsorbed CO and oxygen species to CO_2 is favored by temperature and by the presence of chemisorbed oxygen atoms. Therefore, the absence of gas-phase CO in our CO_2 pulse experiments (without CH_4) can be explained by very fast kinetics of recombination of surface CO and oxygen species.

3.5. Microkinetic Analysis of CH_4, O_2, and CO_2 Activation. On the basis of the above mechanistic analysis and literature data[6,41−43,47−51] we developed microkinetic models (Table 1) and applied them for kinetic evaluation of experimental responses of O_2, CH_4, and CO_2. In order to exclude the effect of possible competition of CH_4 and O_2/CO_2 for the same active sites, we used O_2 and CO_2 responses recorded after pulsing of O_2/Ar = 1:1 and CO_2/Ar = 1:1 mixtures, respectively. Under consideration of the results of the simulation-free analysis of O_2 adsorption in section 3.4 and literature data,[41−43] scheme 2 in Table 1 was chosen to describe O_2 interaction with differently sized Rh NP. The reaction steps considered in this scheme include: (i) adsorption and desorption of molecular oxygen, (ii) reversible dissociation of molecularly adsorbed oxygen species into two atomically adsorbed ones. This model describes well the experimental O_2 responses as exemplary shown in Figure S7 in the SI for the catalysts with Rh NP of 1.1 and 5.5 nm. The obtained kinetic parameters of each individual reaction step are summarized in Table 2.

Table 1. Micro-Kinetic Models Applied for Kinetic Modeling of CH_4, O_2, and CO_2 Activation

model	elementary reaction step	related rate constants/s^{-1}
1	$CH_4 + z \rightarrow$ reaction products	$k^{eff}_{reac}(CH_4)^a$
2	$O_2 + z \rightarrow z\_O_2$	$k^{eff}_{ads}(O_2)^a$
	$z\_O_2 \rightarrow O_2 + z$	$k_{des}(O_2)$
	$z\_O_2 + z \rightarrow 2z\_O$	$k^{eff}_{diss}(O_2)^a$
	$2z\_O \rightarrow z\_O_2 + z$	$k_{ass}(O_2)^b$
3	$CO_2 + z \rightarrow z\_CO_2$	$k^{eff}_{ads}(CO_2)^a$
	$z\_CO_2 \rightarrow CO_2 + z$	$k_{des}(CO_2)$
	$z\_CO_2 + z \rightarrow z\_O + z\_CO$	$k^{eff}_{diss}(CO_2)^a$
	$z\_O + z\_CO \rightarrow z\_CO_2 + z$	$k_{ass}(CO_2)^b$

$^a k^{eff}_{ads} = C_z \cdot k_{ads}$, $k^{eff}_{diss} = C_z \cdot k_{dis}$ (C_z = concentration of active sites). $^b k_{ass}$/m^3_{cat} mol^{-1} s^{-1}.

Table 2. Kinetic Parameters of O_2 Activation over Rh/γ-Al_2O_3 Catalysts Possessing Differently Sized Rh NP

catalyst	$k^{eff}_{ads}(O_2)$/s^{-1}	$k_{des}(O_2)$/s^{-1}	$k^{eff}_{diss}(O_2)$/s^{-1}	$k_{ass}(O_2)$/m^3_{cat}·mol^{-1}·s^{-1}
Rh NP (1.1 nm)/γ-Al_2O_3	$7.4\cdot10^3$	9.7	$7.3\cdot10^1$	$3.7\cdot10^2$
Rh NP (2.5 nm)/γ-Al_2O_3	$5.2\cdot10^3$	$1.4\cdot10^2$	$4.9\cdot10^1$	$7.4\cdot10^2$
Rh NP (2.9 nm)/γ-Al_2O_3	$4.3\cdot10^3$	$7.4\cdot10^1$	$1.1\cdot10^2$	$2.6\cdot10^2$
Rh NP (3.7 nm)/γ-Al_2O_3	$2.6\cdot10^3$	3.2	$2.0\cdot10^2$	$1.3\cdot10^1$
Rh NP (5.5 nm)/γ-Al_2O_3	$1.0\cdot10^3$	2.7	$1.1\cdot10^2$	$1.0\cdot10^1$

Due to a correlation between C_z (total concentration of active sites) and the rate constants of adsorption and dissociation, only their products could be determined, i.e. $k^{eff}_{ads}(O_2) = k_{ads}(O_2)\cdot C_z$ and $k^{eff}_{diss}(O_2) = k_{diss}(O_2)\cdot C_z$. The former constant correlates with the size of Rh NP; the smaller the NP, the higher the $k^{eff}_{ads}(O_2)$ value. Under consideration that all surface Rh atoms (Figure 1) are equivalently active for oxygen adsorption, this correlation will also be valid for $k_{ads}(O_2)$ because $k^{eff}_{ads}(O_2)$ decreases by a factor of 7.4, while the number of surface Rh atoms reduces by a factor of 2.2 upon an increase in Rh NP size from 1.1 to 5.5 nm. The constant of recombination of two atomically adsorbed oxygen species also decreases with the size. The constant of dissociation of molecular adsorbed oxygen species is rather size-insensitive. Surprisingly, the constant of desorption of these species increases from 9.7 to 140 s^{-1} when the size of Rh NP increases from 1.1 to 2.5 and then gradually decreases with a further increase in the size. This is probably due to the fact that very small NP show high oxygen affinity as indirectly supported by the high ratio of $k^{eff}_{ads}(O_2)/k_{des}(O_2)$ and previously results of Ligthart et al.[5] Those authors established that the smaller the Rh NP are, the easier is their oxidation under conditions of methane steam reforming.

On the basis of the above discussion we suggest that the ability of differently sized Rh NP for adsorption and dissociation of gas-phase O_2 is influenced by interplay between the rate constants of individual reaction steps, but not by their

dx.doi.org/10.1021/cs5002465 | ACS Catal. 2014, 4, 3136−3144

absolute values. To illustrate this statement, we calculated the ratio of steady-state coverage by molecularly adsorbed oxygen species to atomically adsorbed ones ($\Theta[O_2]/\Theta[O]$) for O_2 adsorption on Rh NP as a function of partial oxygen pressure. To this end, we used mechanistic scheme 2 in Table 1 and the corresponding rate constants in Table 2. The obtained results are presented in Figure 7.

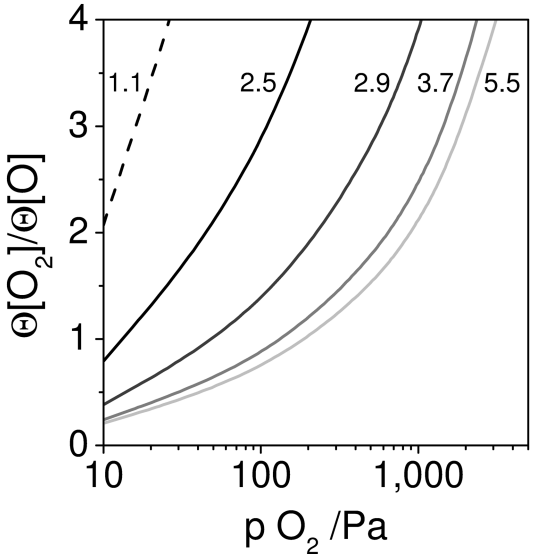

Figure 7. Effect of partial O_2 pressure on the ratio of steady-state coverage by molecularly adsorbed oxygen species to atomic ones estimated using kinetic parameters in Table 2. The numbers in the plot represent the diameter of Rh NP on γ-Al_2O_3 in nm.

It is obvious that this ratio increases with partial pressure of O_2. This means that the coverage by adsorbed oxygen molecules will decrease with a decrease in the pressure and be negligible below 0.01 Pa. This is an agreement with several studies on O_2 adsorption over different Rh single crystals in ultrahigh vacuum;[41,52,53] molecular adsorbed oxygen species were never observed under such conditions at temperatures relevant for this study. It is important to highlight that the smaller the NP, the higher is the $\Theta[O_2]/\Theta[O]$ ratio in the whole pressure range. This means that large Rh NP more easily dissociate molecularly adsorbed oxygen species to atomic ones than their small counterparts. This conclusion agrees well with theoretical predictions of van Santen.[11] In order to activate π bonds as in O_2, a reaction center with unique configuration of several metals atoms is required. The concentration of such centers increases with NP size.

Model 3 in Table 1 describes well the experimental responses of CO_2 (Figure S8 in the SI). This model predicts that CO_2 adsorbs reversibly. The molecular adsorbed CO_2 species can dissociate to adsorbed CO and O, which can recombine. The kinetic parameters of each individual reaction step are listed in Table 3. Similar to the kinetic constants of O_2 activation, those of adsorption and dissociation of CO_2 correlate with the total concentration of active sites (C_z). As a consequence, it was possible to determine only a product of these two parameters, i.e. $k^{eff}_{ads}(CO_2) = k_{ads}(CO_2)\cdot C_z$ and $k^{eff}_{diss}(CO_2) = k_{diss}(CO_2)\cdot C_z$. It appears that the apparent adsorption constant decreases with increasing size of Rh NP, while no definitive relations were established for other rate constants.

Table 3. Kinetic Parameters of CO_2 Activation over Rh/γ-Al_2O_3 Catalysts Possessing Differently Sized Rh NP

catalyst	$k^{eff}_{ads}(CO_2)$/ s^{-1}	$k_{des}(CO_2)$/ s^{-1}	$k^{eff}_{diss}(CO_2)$/ s^{-1}	$k_{ass}(CO_2)$/ $m^3_{cat}\cdot mol^{-1}\cdot s^{-1}$
Rh NP (1.1 nm)/ γ-Al_2O_3	$1.0\cdot10^3$	$1.2\cdot10^2$	$1.0\cdot10^1$	$6.6\cdot10^3$
Rh NP (2.5 nm)/ γ-Al_2O_3	$9.1\cdot10^2$	$4.4\cdot10^2$	5.4	$3.8\cdot10^3$
Rh NP (2.9 nm)/ γ-Al_2O_3	$9.7\cdot10^2$	$2.0\cdot10^2$	6.4	$5.5\cdot10^3$
Rh NP (3.7 nm)/ γ-Al_2O_3	$8.9\cdot10^2$	$1.3\cdot10^2$	6.0	$5.3\cdot10^3$
Rh NP (5.5 nm)/ γ-Al_2O_3	$6.8\cdot10^2$	$5.4\cdot10^2$	6.4	$3.2\cdot10^2$

Since breaking of the C−H bond in CH_4 is the rate-limiting step, we considered only CH_4 interaction with an active site, i.e. one-step irreversible reaction of CH_4 (model 1 in Table 1). An apparent first-order constant of this interaction was obtained from eq 6 according to the so-called thin-zone TAP reactor model.[54] This constant has the unit of s^{-1} and can be interpreted as turnover frequency of methane conversion.

$$X(CH_4) = \frac{k_{CH_4}\cdot\varepsilon_b\cdot(\Delta L\cdot L_{II}/D_{eff})}{1 + k_{CH_4}\cdot\varepsilon_b\cdot(\Delta L\cdot L_{II}/D_{eff})} \quad (6)$$

where $X(CH_4)$ and k_{CH_4} are the conversion of CH_4 and the corresponding apparent constant. ΔL and L_{II} are lengths of the catalyst layer and the second inert zone, respectively. D_{eff} is an effective diffusion coefficient of CH_4. ε_b is the fractional voidage of the packed bed in the reactor.

The conversion of CH_4 was determined from its inlet and outlet concentrations. Its diffusion coefficient was calculated from the diffusion coefficient of Ar pulsed together with CH_4. It is beyond the scope of our approach to consider the structure of the active sites or the charge of oxygen species responsible for CH_4 oxidation in the presence of O_2 or CO_2. The obtained apparent first-order kinetic constants for breaking the C−H bond in the methane molecule in the presence and the absence of O_2 or CO_2 are summarized in Figure 8. It is obvious that the constant of CH_4 activation in the absence of oxidizing agent decreases with an increase in the size of Rh NP. According to van Santen,[11] such decrease can be explained by the fact that surface atoms at the edges of Rh NP are required for activation of a σ bond like a C−H bond in CH_4; the smaller the particles, the higher the concentration of such atoms.

When CH_4 was activated in the presence of O_2 or CO_2 over catalysts possessing Rh NP of 1.1, 2.5, or 2.9 nm, the obtained rate constants are close to those determined in the absence of these oxidizing agents and also decrease with an increase in the size of Rh NP. Compared to oxidant-free CH_4 activation, the apparent rate constant of CH_4 conversion with O_2 or CO_2 over the catalysts possessing Rh NP of 3.7 or 5.5 nm increased (Figure 8). However, in agreement with oxidant-free tests, the former NP are more active than the latter, i.e. O_2 or CO_2 does not change the negative effect of NP size on methane activation.

The increase in the apparent rate constant of CH_4 conversion on 3.7 or 5.5 nm Rh NP in the presence of oxidizing agents is probably related to experimental peculiarities of our tests. Owing to the different number of surface Rh atoms in differently sized Rh NP, the ratio of pulsed CH_4 to these atoms increased from approximately 1 to 2 upon increasing NP size from 1.1 to 5.5 nm, respectively. Consequently, the effect

dx.doi.org/10.1021/cs5002465 | ACS Catal. 2014, 4, 3136−3144

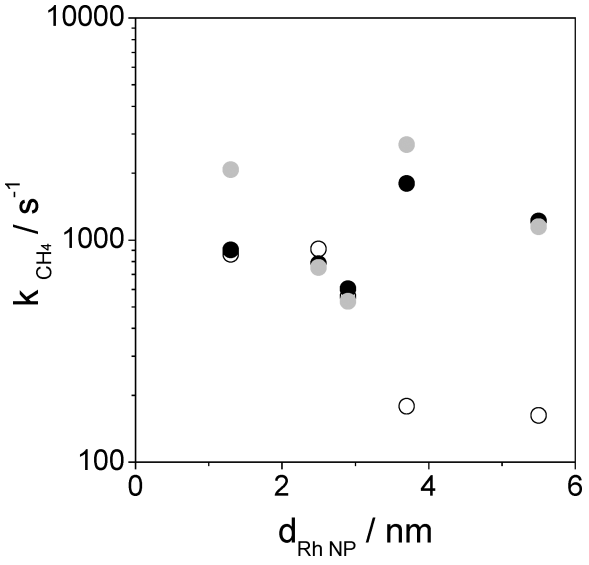

Figure 8. Apparent rate constant of CH_4 activation over differently sized Rh NP on γ-Al_2O_3 as determined from CH_4/Ar = 1:1 (○), CH_4/O_2/Ar = 2:1:2 (●) and CH_4:CO_2/Ar = 1:1:1 (●) experiments according to procedure described in ref 14.

of copulsed O_2 or CO_2 on the generation of active oxygen species required for methane activation should be more marked for catalysts possessing large Rh NP, i.e. with low concentration of surface Rh atoms. Moreover, the analysis of data shown in Table 2 and Table 3 indicates that for both O_2 and CO_2 activation, the ratio of k_{ads}^{eff}/k_{des} decreases with an increase in NP diameter from 1.1 to 2.9 nm but rises with a further increase in the Rh NP size. The apparent rate of CH_4 activation in the presence of O_2 or CO_2 behaves very similarly (Figure 8). Formally the ratio of k_{ads}^{eff}/k_{des} suggests an accumulation of active O-containing species on the NP surface. This effect under transient vacuum conditions will be again pronounced for catalysts with a low number of surface Rh atoms, i.e. for those possessing large Rh NP. Therefore, only the kinetic constants of CH_4 activation over Rh NP in the absence of any oxidant reflect their intrinsic activity for breaking of the C−H bond.

3.6. Kinetic Origins of the Effect of the Size of Supported Rh NP on POM Performance. As demonstrated in sections 3.2 and 3.3, Rh NP size strongly influences the activity (Figure 4) and selectivity (Figure 2) of POM over Rh/γ-Al_2O_3 but not the overall reaction scheme (Figure 3). On the basis of our and several previous studies, POM can be divided into two regimes, depending on oxygen partial pressure: (i) CO_2 (mainly), CO (partly) and H_2O are the only products of CH_4 oxidation in the presence of gas-phase O_2 (upper part of the catalyst layer); (ii) when O_2 is completely consumed, dry and steam reforming of methane results in CO and H_2 downstream to the catalyst bed. It is reasonable to suggest that catalyst activity in the first zone is governed by the rates of CH_4 and O_2 activation, while the ability of the catalyst for CH_4 and CO_2 activation should determine the activity in the second zone. As shown in Figure 8, the rate constant of methane decomposition over metallic Rh sites decreases with an increase in NP size. A similar behavior was also identified for the apparent constant of O_2 adsorption ($k_{ads}^{eff}(O_2)$ in Table 2). Formally, the higher the constant, the faster the generation of adsorbed oxygen species required for CO_x formation from CH_4. It is also worth mentioning that differently sized Rh NP differ in their ability to generate biatomic and monatomic surface oxygen species formed upon activation of gas-phase O_2. For a broad range of partial O_2 pressures, our kinetic modeling predicts an increase in the ratio of $\Theta[O_2]/\Theta[O]$ (Figure 7) with a decrease in the size of Rh NP. On the basis of DFT analysis, Chin et al.[10] considered pair oxygen species for methane oxidation over supported Pt NP.[10] Biatomic oxygen species were also suggested to be responsible for total oxidation of methane[55,56] and propane[57] over oxide-based catalysts. Considering these literature data, we also assume that Rh sites with two neighboring oxygen species (biatomic or pair sites) participate in total oxidation of surface CH_x fragments to CO_2 and H_2O in the course of POM over Rh/γ-Al_2O_3. Since the concentration of biatomic oxygen species and the rate constants of O_2 (Table 2) and CH_4 (Figure 8) activation increase with a decrease in Rh NP size, the rate of CH_4 oxidation to CO_2 formation should also rise accordingly. For steady-state operation at a certain constant contact time (fixed total catalyst layer and feed flow), this means that the zone of Rh/γ-Al_2O_3 required for complete conversion of O_2 will be shorter for smaller than for larger Rh NP. Consequently, a larger part of the downstream catalyst layer is available for CH_4-reforming reactions. In addition, the turnover rate of the generation of adsorbed CO_x species from gas-phase CO_2 ($k_{ads}^{eff}(CO_2)$ in Table 3) increases with a decrease in NP size. As shown in section 3.3, such species are reduced by adsorbed hydrogen or methane species to yield carbon monoxide. Thus, the reforming reactions should also run faster on small NPs in agreement with previous studies on steam[4−7] and dry[7,8,58] reforming of methane. Therefore, the size of Rn NP positively influences both their activity for complete conversion of methane to CO_x and H_2O in the presence of gas-phase O_2 and for methane reforming reactions in the absence of O_2 to yield synthesis gas.

4. CONCLUSIONS

In this work we demonstrated that Rh(0.005 wt %)/γ-Al_2O_3 catalysts possessing well-defined colloidally prepared Rh NP (1.1, 2.5, 2.9, 3.7, and 5.5 nm) strongly differ in their activity and selectivity in partial oxidation of methane to syngas. The larger the particles, the lower are the yield of CO and the ratio of H_2/CO obtained. Steady-state tests and transient experiments with submillisecond time resolution proved that the overall scheme of products formation does not depend on NP size. CO is mainly formed through reforming reactions of CH_4 with CO_2 and H_2O. However, the reaction pathway yielding hydrogen is decoupled from that of CO.

Our detailed microkinetic analysis enabled us to conclude that the mechanism of CH_4, O_2, and CO_2 activation does not depend on NP size. However, the kinetics of these processes is size-dependent and thus governs the POM performance of supported Rh NP. This knowledge provides hints for prediction of cluster effects on POM performance of catalysts possessing supported metal species and opens the possibility for tuning their activity and, most importantly, selectivity via the size of supported nanoparticles.

■ ASSOCIATED CONTENT

Supporting Information

Data of SAXS and N_2O titration measurements; steady-state CO selectivity and ratio of H_2:CO; transient responses of feed components and reaction products after different pulse experiments in the TAP reactor; experimental and simulated

dx.doi.org/10.1021/cs5002465 | ACS Catal. 2014, 4, 3136−3144

responses of O_2 and CO_2. This material is available free of charge via the Internet at http://pubs.acs.org.

AUTHOR INFORMATION

Corresponding Author

*Evgenii.kondratenko@catalysis.de (E.V.K.)

Notes

The authors declare no competing financial interest.

ACKNOWLEDGMENTS

Dr. Norbert Steinfeldt is gratefully acknowledged for the assistance in the synthesis of supported Rh nanoparticles. This manuscript is dedicated to Professor Dr. Manfred Baerns on the occasion of his 80th birthday.

REFERENCES

(1) Enger, B. C.; Lodeng, R.; Holmen, A. *Appl. Catal., A* **2008**, *346*, 1.
(2) York, A. P. E.; Xiao, T.; Green, M. L. H. *Top. Catal.* **2003**, *22*, 345.
(3) Zhu, Q.; Zhao, X.; Deng, Y. *J. Nat. Gas Chem.* **2004**, *13*, 191.
(4) Jones, G.; Jakobsen, J. G.; Shim, S. S.; Kleis, J.; Andersson, M. P.; Rossmeisl, J.; Abild-Pedersen, F.; Bligaard, T.; Helveg, S.; Hinnemann, B.; Rostrup-Nielsen, J. R.; Chorkendorff, I.; Sehested, J.; Nørskov, J. K. *J. Catal.* **2008**, *259*, 147.
(5) Ligthart, D. A. J. M.; Van Santen, R. A.; Hensen, E. J. M. *J. Catal.* **2011**, *280*, 206.
(6) Wei, J.; Iglesia, E. *Angew. Chem., Int. Ed.* **2004**, *43*, 3685.
(7) Wei, J.; Iglesia, E. *J. Catal.* **2004**, *225*, 116.
(8) Wei, J.; Iglesia, E. *J. Phys. Chem. B* **2004**, *108*, 4094.
(9) Chin, Y.-H.; Buda, C.; Neurock, M.; Iglesia, E. *J. Am. Chem. Soc.* **2011**, *133*, 15958.
(10) Chin, Y.-H.; Buda, C.; Neurock, M.; Iglesia, E. *J. Catal.* **2011**, *283*, 10.
(11) Van Santen, R. A. *Acc. Chem. Res.* **2008**, *42*, 57.
(12) Berger-Karin, C.; Sebek, M.; Pohl, M.-M.; Bentrup, U.; Kondratenko, V. A.; Steinfeldt, N.; Kondratenko, E. V. *ChemCatChem.* **2012**, *4*, 1368.
(13) Liao, M.-S.; Zhang, Q.-E. *J. Mol. Catal.* **1998**, *136*, 185.
(14) Gleaves, J. T.; Yablonsky, G. S.; Phanawadee, P.; Schuurman, Y. *Appl. Catal., A* **1997**, *160*, 55.
(15) Pérez-Ramírez, J.; Kondratenko, E. V. *Catal. Today* **2007**, *121*, 160.
(16) Soick, M.; Wolf, D.; Baerns, M. *Chem. Eng. Sci.* **2000**, *55*, 2875.
(17) Sinkovek, R. F.; Madsen, N. K. *ACM Trans. Math. Software* **1975**, *1*, 232.
(18) Baerns, M.; Buyevskaya, O. V.; Mleczko, L.; Wolf, D. *Stud. Surf. Sci. Catal.* **1997**, *107*, 421.
(19) Press, W. H.; Flannery, B. P.; Teukolsky, S. A.; Vetterling, W. T. *Numerical Recipes in FORTRAN*, 2nd ed.; Cambridge University Press: Cambridge, 1992.
(20) Fritz, G.; Bergmann, A.; Glatter, O. *J. Chem. Phys.* **2000**, *113*, 9733.
(21) Glatter, O. *J. Appl. Crystallogr.* **1977**, *10*, 415.
(22) *V. PCG Software Package*, University Graz.
(23) Wider, J.; Greber, T.; Wetli, E.; Kreutz, T. J.; Schwaller, P.; Osterwalder, J. *Surf. Sci.* **1998**, *417*, 301.
(24) Peterlinz, K. A.; Sibener, S. J. *J. Phys. Chem.* **1995**, *99*, 2817.
(25) Benfield, R. E. *J. Chem. Soc., Faraday Trans.* **1992**, *88*, 1107.
(26) Lee, I.; Delbecq, F.; Morales, R.; Albiter, M. A.; Zaera, F. *Nat. Mater.* **2009**, *8*, 132.
(27) Tsung, C.-K.; Kuhn, J. N.; Huang, W.; Aliaga, C.; Hung, L.-I.; Somorjai, G. A.; Yang, P. *J. Am. Chem. Soc.* **2009**, *131*, 5816.
(28) Prieto, P. J. S.; Ferreira, A. P.; Haddad, P. S.; Zanchet, D.; Bueno, J. M. C. *J. Catal.* **2010**, *276*, 351.
(29) Horn, R.; Williams, K. A.; Degenstein, N. J.; Bitsch-Larsen, A.; Dalle Nogare, D.; Tupy, S. A.; Schmidt, L. D. *J. Catal.* **2007**, *249*, 380.
(30) Horn, R.; Williams, K. A.; Degenstein, N. J.; Schmidt, L. D. *J. Catal.* **2006**, *242*, 92.
(31) Mallens, E. P. J.; Hoebnik, J. H. B. J.; Marin, G. B. *J. Catal.* **1997**, *167*, 43.
(32) Hickman, D. A.; Schmidt, L. D. *Science* **1993**, *259*, 343.
(33) Liu, Y.; Huang, F.-Y.; Li, J.-M.; Weng, W.-Z.; Luo, C.-R.; Wang, M.-L.; Xia, W.-S.; Huang, C.-J.; Wan, H.-L. *J. Catal.* **2008**, *256*, 192.
(34) Buyevskaya, O. V.; Walter, K.; Wolf, D.; Baerns, M. *Catal. Lett.* **1996**, *38*, 81.
(35) Berger-Karin, C.; Radnik, J.; Kondratenko, E. V. *J. Catal.* **2011**, *280*, 116.
(36) Berger-Karin, C.; Wohlrab, S.; Rodemerck, U.; Kondratenko, E. V. *Catal. Commun.* **2012**, *18*, 121.
(37) Salazar-Villalpando, M. D.; Berry, D. A.; Cugini, A. *Int. J. Hydrogen Energy* **2010**, *35*, 1998.
(38) Dubois, L. H.; Somorjai, G. A. *Surf. Sci.* **1979**, *88*, L13.
(39) Kondratenko, E. V.; Wang, H. H.; Kondratenko, V. A.; Caro, J. *J. Mol. Catal. A: Chem.* **2009**, *297*, 142.
(40) Sadykov, V. A.; Sazonova, N. N.; Bobin, A. S.; Muzykantov, V. S.; Gubanova, E. L.; Alikina, G. M.; Lukashevich, A. I.; Rogov, V. A.; Ermakova, E. N.; Sadovskaya, E. M.; Mezentseva, N. V.; Zevak, E. G.; Veniaminov, S. A.; Muhler, M.; Mirodatos, C.; Schuurman, Y.; van Veen, A. C. *Catal. Today* **2011**, *169*, 125.
(41) Fisher, G. B.; Schmieg, S. J. *J. Vac. Sci. Technol.* **1983**, *A1*, 1064.
(42) German, E.; Efremenko, I. *J. Mol. Struct. (THEOCHEM)* **2004**, *711*, 159.
(43) German, E. D.; Sheintuch, M. *Russ. J. Phys. Chem.* **2007**, *1*, 357.
(44) Bradley, J. M.; Guo, X.-C.; Hopkinson, A.; King, D. A. *J. Chem. Phys.* **1996**, *104*, 4283.
(45) Groß, A.; Eichler, A.; Hafner, J.; Mehl, M. J.; Papaconstantopoulos, D. A. *Surf. Sci.* **2003**, *539*, L542.
(46) Abramova, L. A.; Zeigarnik, A. V.; Baranov, S. P.; E, S. *Surf. Sci.* **2004**, *565*, 45.
(47) Castner, D. G.; Sexton, B. A.; Somorjai, G. A. *Surf. Sci.* **1978**, *71*, 519.
(48) Castner, D. G.; Somorjai, G. A. *Surf. Sci.* **1979**, *83*, 60.
(49) Dubois, L. H.; Somorjai, G. A. *Surf. Sci. Lett.* **1980**, *91*, A18.
(50) Hendrickx, H. A. C. M.; Jongenelis, A. P. J. M.; Nieuwenhuys, B. E. *Surf. Sci.* **1985**, *154*, 503.
(51) van Tol, M. F. H.; Gielbert, A.; Nieuwenhuys, B. E. *Appl. Surf. Sci.* **1993**, *67*, 166.
(52) Belton, D. N.; Fisher, G. B.; DiMaggio, C. L. *Surf. Sci.* **1990**, *233*, 12.
(53) Comelli, G.; Dhanak, V. R.; Kiskinova, M.; Pangher, N.; Paolucci, G.; Prince, K. C.; Rosei, R. *Surf. Sci.* **1992**, *260*, 7.
(54) Shekhtman, S. O.; Yablonsky, G. S.; Chen, S.; Gleaves, J. T. *Chem. Eng. Sci.* **1999**, *54*, 4371.
(55) Kondratenko, E. V.; Buyevskaya, O.; Baerns, M. *J. Mol. Catal. A: Chem.* **2000**, *158*, 199.
(56) Kondratenko, E. V.; Buyevskaya, O.; Soick, M.; Baerns, M. *Catal. Lett.* **1999**, *63*, 153.
(57) Rozanska, X.; Kondratenko, E. V.; Sauer, J. *J. Catal.* **2008**, *256*, 84.
(58) Wei, J.; Iglesia, E. *J. Phys. Chem. B* **2004**, *108*, 7253.